HHS Public Access

Author manuscript

Cell. Author manuscript; available in PMC 2023 December 08.

Published in final edited form as:

Cell. 2022 December 08; 185(25): 4801–4810.e13. doi:10.1016/j.cell.2022.10.024.

Structural basis for the severe adverse interaction of sofosbuvir and amiodarone on L-type Ca_v channels

Xia Yao[1,5], **Shuai Gao**[1,5,7,9], **Jixin Wang**[2,6], **Zhangqiang Li**[3,6], **Jian Huang**[1], **Yan Wang**[4], **Zhifei Wang**[4], **Jiaofeng Chen**[3], **Xiao Fan**[1], **Weipeng Wang**[3], **Xueqin Jin**[3], **Xiaojing Pan**[3], **Yong Yu**[4], **Armando Lagrutta**[2], **Nieng Yan**[1,8,9]

[1]Department of Molecular Biology, Princeton University, Princeton, NJ 08544, USA

[2]Department of Genetic and Cellular Toxicology, ADME & Discovery Toxicology, Preclinical Development, Merck Research Laboratories, Merck & Co., Inc., West Point, PA 19486, USA

[3]State Key Laboratory of Membrane Biology, Beijing Advanced Innovation Center for Structural Biology, Tsinghua-Peking Joint Center for Life Sciences, School of Life Sciences, Tsinghua University, Beijing 100084, China

[4]Department of Biological Sciences, St. John's University, Queens, NY 11439, USA

[5]These authors contribute equally.

[6]These authors contribute equally.

[7]Present address: School of Pharmaceutical Sciences, TaiKang Center for Life and Medical Sciences, Wuhan University, Wuhan 430071, China

[8]Lead contact.

Summary

Drug-drug interaction of the antiviral sofosbuvir and the antiarrhythmics amiodarone has been reported to cause fatal heartbeat slowing. Sofosbuvir and its analog, MNI-1, were reported to potentiate the inhibition of cardiomyocyte calcium handling by amiodarone, which functions as a multi-channel antagonist, and implicate its inhibitory effect on L-type Ca_v channels, but the molecular mechanism has remained unclear. Here we present systematic cryo-EM structural analysis of $Ca_v1.1$ and $Ca_v1.3$ treated with amiodarone or sofosbuvir alone, or sofosbuvir/MNI-1 combined with amiodarone. Whereas amiodarone alone occupies the dihydropyridine binding site, sofosbuvir is not found in the channel when applied on its own. In the presence of amiodarone, sofosbuvir/MNI-1 is anchored in the central cavity of the pore domain through specific interaction

[9]To whom correspondence should be addressed: N. Yan (nyan@princeton.edu); S. Gao (gaoshuai812@whu.edu.cn).

Author Contributions

N.Y. conceived the project. X.Y., and S.G. conducted cryo-EM studies. J.W. and A.L. conducted $Ca_V1.2$ calcium influx experiments. Z.L., X.F. and W.W. helped cryo-EM analyses. J.H. performed molecular docking simulation. Y.Y., Y.W., Z.W., J.C., X.J., and X.P. helped functional characterizations. All authors contributed to data analysis and manuscript preparation. N.Y., X.Y., and S.G. wrote the manuscript.

Declaration of interests

Jixin Wang and Armando Lagrutta are employees of Merck Sharp & Dohme LLC, a subsidiary of Merck & Co., Inc., Rahway, NJ, USA and potentially own stock and/or hold stock options in Merck & Co., Inc., Rahway, NJ, USA.

with amiodarone and directly obstructs the ion permeation path. Our study reveals the molecular basis for the physical, pharmacodynamic interaction of two drugs on the scaffold of Ca_v channels.

Keywords

Sofosbuvir; Amiodarone; Drug safety; Drug-drug interactions; Severe bradycardia; L-type Ca_v channels; Cryo-EM; $Ca_v1.1$; $Ca_v1.3$; Voltage-gated calcium channels

Introduction

Sofosbuvir (or Sovaldi, short as SOF, Figure 1A), approved by the US Food and Drug Administration in 2013, has been an effective drug for the treatment of hepatitis C (Afdhal et al., 2014; Jacobson et al., 2013; Lawitz et al., 2013; Mangia et al., 2020). In 2015, severe slowing of heartbeat rate, including one fatal, was reported in patients following coadministration of SOF and amiodarone (AMIO, Figure 1A), a class III antiarrhythmic agent for the treatment of ventricular arrhythmias and atrial fibrillation (Back and Burger, 2015). SOF is a nucleotide analog inhibitor targeting Nonstructural protein 5B (NS5B) RNA polymerase of hepatitis C virus (HCV), and AMIO is a multi-channel blocker that can act on Ca^{2+}, Na^+, and K^+ channels (Appleby et al., 2015; Kodama et al., 1997; Roy et al., 2000; Stedman, 2014). Ensuing investigations showed that SOF or its analog, MNI-1 (MRL, Merck & Co., Rahway, NJ, USA, Figure 1A), potentiated calcium-handling effects by AMIO in human cardiomyocytes, and increased AMIO's inhibition of L-type Ca^{2+} channels (LTCC) (Lagrutta et al., 2017; Lagrutta et al., 2016; Millard et al., 2016). However, the underlying molecular mechanism was not clear.

LTCCs, also known as the dihydropyridine receptors (DHPR), refer to the Ca_v1 subfamily of the voltage-gated Ca^{2+} channels (Carbone and Lux, 1984; Dolphin, 2006; Ertel et al., 2000; Kohlhardt and Fleckenstein, 1977; Nowycky et al., 1985). LTCCs are heteromeric channels consisting of a core α1 subunit, an extracellular α2δ subunit, an intracellular β subunit, and in some complexes a transmembrane γ subunit. Classification of Ca_v channels is based on the α1 subunit, which comprises four repeats each containing six transmembrane segments S1-S6 (Ertel et al., 2000). The S1-S4 segments in each repeat constitute the voltage-sensing domain (VSD), which undergoes conformational changes in response to fluctuations of the membrane potential. And the S5 and S6 segments of the four repeats enclose the central pore domain (PD) that is responsible for selective Ca^{2+} conductance (Tanabe et al., 1987; Wu et al., 2015).

Among the four Ca_v1 members, $Ca_v1.1$ is specialized for excitation-contraction coupling (ECC) of skeletal muscles; $Ca_v1.4$ predominantly functions in retina, playing a critical role for neurotransmitter release; and $Ca_v1.2$ and $Ca_v1.3$ exhibit a more diverse tissue distribution in heart, brain, and endocrine cells. Dysfunction of $Ca_v1.2$ and $Ca_v1.3$ has been characterized in various arrythmias. $Ca_v1.2$ controls ECC of cardiomyocytes, and $Ca_v1.3$, the primary subtype in the sinoatrial node and the atrioventricular node, is required for the pacemaker activity (Zamponi et al., 2015). Consistently, DDI of SOF/MNI-1 and AMIO interferes with calcium handling in cardiomyocyte models and $Ca_v1.2$ and $Ca_v1.3$ channel activity (Lagrutta et al., 2017; Lagrutta et al., 2016; Millard et al., 2016).

To dissect the molecular basis for the DDI of SOF/MNI-1 and AMIO on $Ca_v1.2$ and $Ca_v1.3$ channels, we set out to solve the structures of LTCCs supplemented with different drug combinations. For a long time, the multi-subunit $Ca_v1.1$ complex isolated from the skeletal muscle of rabbits, designated $rCa_v1.1$, has been a prototype for structural analysis of LTCC modulation by various anti-hypertension agents, such as DHP drugs and pore blockers (Gao and Yan, 2021; Wu et al., 2016; Zhao et al., 2019). Because of the high sequence similarity among the LTCC members, we first collected cryo-EM data for $rCa_v1.1$ treated with AMIO, or AMIO combined with MNI-1 (short as AM). To study the DDI on the physiologically more relevant human LTCCs, we managed to obtain the human ternary $Ca_v1.3$ complex, consisting of α1, α2δ-1, and β3 subunits, through recombinant expression in HEK293 cells (Yao et al., 2022). Cryo-EM data were collected for $Ca_v1.3$ separately incubated with AMIO, SOF, and AMIO together with SOF (short as AS).

Our systematic structural analyses demonstrate that AMIO alone inserts into the pore fenestration enclosed by repeat III and IV of LTCCs. Alone, neither SOF nor MNI-1 can bind to the channels; in the presence of AMIO however, either SOF or MNI-1 is able to act as a pore blocker that directly cuts off the ion permeation path in the central cavity of the channel. Our study reveals direct physical interaction of two small molecule blockbuster drugs within the scaffold of a protein, leading to clinically meaningful drug-drug interaction.

Results

Synergistic DDI of AMIO and MNI-1

Expanding on previously published data (Lagrutta et al., 2017; Millard et al., 2016), we used a HEK293 cell line that stably overexpresses human $Ca_v1.2$ channels for functional investigations of DDI. The pharmacodynamic interactions of MNI-1 with AMIO, or with two other LTCC blockers, nifedipine and verapamil, were separately explored. MNI-1 alone inhibited $Ca_v1.2$ with an IC_{50} value of more than 100 μM (Figure 1B). The dramatically enhanced inhibition by co-applied MNI-1 and AMIO indicates a strong synergistic effect between these two drugs (Figure 1C). In contrast, MNI-1 shows no synergistic interaction with nifedipine or verapamil (Figures S1A,B).

We modelled the effect of different Ca_v inhibitors tested on MNI-1 (Figure 1D; Figure S1C). In general, for two compounds that inhibit Ca^{2+} influx independently, the individual inhibition by one compound would match the total effect subtracted from the portion of blockage by the other compound, as seen in the modelling of no interaction between nifedipine and MNI-1 (Figure 1D; Figure S1C, middle). For AMIO, the experimental MNI-1 inhibition in the combination assays is consistently higher than predicted values, in accordance with the synergistic DDI of these two drugs (Figure 1D; Figure S1C, left). In contrast, the inhibition of $Ca_v1.2$ by MNI-1 was modelled to be diminished by verapamil at high concentrations, suggesting a competition between the two drugs for pore blocking (Figure 1D; Figure S1C, right).

Inspired by the synergistic DDI of MNI-1 and AMIO, we sought to employ the cryo-EM technology to examine the potential association of AMIO and MNI-1 with LTCCs.

Structural analysis of rCa$_v$1.1 bound to AMIO and MNI-1

Purification of rCa$_v$1.1 was performed following our reported protocol (Gao and Yan, 2021; Wu et al., 2016). For structural analysis of rCa$_v$1.1 in the presence of AMIO alone or in combination with MNI-1, AMIO was supplemented at a final concentration of 0.1 mM, and a titration of MNI-1 at 0.1 mM and 1 mM was used. After incubation at 4 °C for 30 min, cryo-grids were prepared for the three samples, referred to as rCa$_v$1.1A for rCa$_v$1.1 with AMIO only, rCa$_v$1.1AM0.1 for AMIO plus 0.1 mM MNI-1, and rCa$_v$1.1AM for AMIO plus 1 mM MNI-1. Following standard image acquisition and processing protocols, 3D EM reconstructions for rCa$_v$1.1A, rCa$_v$1.1AM0.1, and rCa$_v$1.1AM were obtained at 2.8 Å, 2.8 Å, and 3.0 Å, respectively (Table 1; Figure S2).

In all three maps, the density for AMIO was well resolved (Figure 1E). When applied at 0.1 mM, MNI-1 could not be reliably built into the discontinuous densities that are adjacent to AMIO (Figure 1E, middle). At 1 mM, a stretch of density that can be well fitted by MNI-1 is unambiguously resolved in the central cavity of the PD (Figure 1E, right). The MNI-1 density in rCa$_v$1.1AM serves as a reference to confirm that the weaker and noisier density in the cavity of rCa$_v$1.1AM0.1 should belong to MNI-1. We next focus on rCa$_v$1.1A and rCa$_v$1.1AM for structural analysis.

Coordination of AMIO by rCa$_v$1.1

AMIO occupies the same site as for DHP compounds, i.e., the III-IV fenestration enclosed by S5$_{III}$, S6$_{III}$, and S6$_{IV}$ (Gao and Yan, 2021; Zhao et al., 2019) (Figure 2A). This observation immediately affords a molecular interpretation for the reported antagonism of the binding of a DHP drug nitrendipine to cardiac LTCC by AMIO (Lubic et al., 1994; Nokin et al., 1986).

Although the overall structures of AMIO- and nifedipine-bound rCa$_v$1.1 are nearly identical, with the root-mean-square deviation (RMSD) of 0.57 Å over 970 superimposed Cα atoms in the α1 subunit (Figure 2B), the coordination modes for the two classes of compounds deviate substantially. Unlike DHP compounds, whose LTCC-specificity is defined by several polar interactions (Gao and Yan, 2021; Zhao et al., 2019), AMIO is surrounded entirely by hydrophobic residues (Figure 2C). The fenestration-encompassing residues on S6$_{III}$ and S6$_{IV}$ are the major contributors for AMIO binding. In addition, Thr1012 and Phe1013 on the first pore helix of repeat III (P1$_{III}$) are in the vicinity of the bound drug, and S5$_{III}$ engages one residue, Val932, for AMIO coordination.

Direct interaction of AMIO and MNI-1 within rCa$_v$1.1

Accommodation of MNI-1 within the central cavity of the PD in the presence of AMIO is consistent with the mode of action (MOA) of a pore blocker (Figure 3A). MNI-1, which lies right below the selectivity filter (SF), stretches from S6$_{II}$ to S6$_{IV}$, traversing the central cavity and contacting all four S6 helices. Scrutiny of MNI-1 coordination affords clues to its unfavored binding to the PD when AMIO is not present.

MNI-1 has a good aqueous solubility of ~ 3 mM. However, the water-soluble molecule is situated in a highly hydrophobic environment in Ca$_v$ proteins (Figure 3B). The incongruent

chemical properties of the ligand and the binding pocket may explain the low potency of MNI-1 on LTCC in the absence of AMIO (Figure 1B). While some of the hydrophobic residues, mainly on the S6 segments in repeats I, III, and IV, contribute to the binding of the hydrophobic groups of the compound (Figure 3B), Leu653 on $S6_{II}$ and Asn1058 on $S6_{III}$ are unfavorably positioned adjacent to the polar and hydrophobic groups of MNI-1, respectively (Figure 3C).

The structure shows that AMIO facilitates the accommodation of MNI-1 into the PD of LTCC by anchoring MNI-1 through direct physical association. In addition to the hydrophobic contacts, there is a polar interaction between the phosphate group of MNI-1 and the tertiary amine of AMIO (Figure 3D). This specific electrostatic coordination may play a critical role for stabilizing MNI-1 in the PD (Figure 3A).

We next examined the molecular basis for the lack of interactions between MNI-1 and nifedipine or verapamil (Figure 1D). For this, we compared the structures of $rCa_v1.1$ bound to nifedipine or verapamil (PDB codes: 6JP5 and 6JPA) with that of $rCa_v1.1$AM. Nifedipine, which is smaller than AMIO (Figure 2B), is distanced from MNI-1 by ~ 7 Å, beyond the range for direct interactions (Figure 3E). Structural comparison also provides an immediate explanation for the competition between verapamil and MNI-1, as their binding poses overlay in the central cavity (Figure 3F). Furthermore, verapamil, with its dominant binding pose revealed in the structure , does not form specific interactions with AMIO (Figure S3), consistent with the lack of synergetic effect between these two drugs (Lagrutta et al., 2016).

Interaction of AMIO and SOF in human $Ca_v1.3$

We then attempted to study the DDI on the physiologically more relevant human LTCCs. Our previously published functional data on HCV prodrugs interacting with AMIO demonstrated similar effects on $hCa_v1.2$ or $hCa_v1.3$ channels (Lagrutta et al., 2017; Millard et al., 2016), and it is likely that $hCa_v1.3$ plays a relevant role in the clinically reported DDI between SOF and AMIO, resulting in the severe bradycardia (Millard et al., 2016). Our recent studies on human $Ca_v2.2$ showed that selection of the β subunit was critical for improving recombinant expression of the channel complex in HEK293F cells (Gao et al., 2021). Indeed, in the presence of β3, which was used for the expression of the $Ca_v2.2$ channel complex, $Ca_v1.3$, together with α2δ-1, can be obtained to sufficient quantity for cryo-EM analysis. However, the expression level of $Ca_v1.2$ complex remained low. Based on these considerations and the high sequence similarity among the Ca_v1 subunits (Figure S4A), we used recombinant $hCa_v1.3$ complex for structural analysis.

SOF differs from MNI-1 only in the substituent on the tetrahydrofuran ring. The fluorine in SOF is replaced by the alkyne group in MNI-1 (Figure 1A). We have solved the following cryo-EM structures: $hCa_v1.3$A for $hCa_v1.3$ with 0.14 mM AMIO at 3.1 Å, $hCa_v1.3$S for $hCa_v1.3$ supplemented with 1.4 mM SOF at 3.3 Å, and $hCa_v1.3$AS for $hCa_v1.3$ with 0.14 mM AMIO and 1.4 mM SOF at 3.3 Å (Table 2; Figures S4, S5). Even in the presence of 1.4 mM SOF, there is no corresponding density in the central cavity of $hCa_v1.3$S (Figure S5A, left). Ligand densities are observed in the other two 3D EM reconstructions.

The three overall structures of $hCa_v1.3$ are nearly identical to that of $rCa_v1.1$. When $hCa_v1.3AS$ is superimposed with $rCa_v1.1AM$, the RMSD for 1782 Cα atoms in α1 and α2δ-1 is 0.66 Å (Figure 4A). Substitution of the alkyne group with fluorine on tetrahydrofuran does not alter the binding mode with LTCCs. Coordination for these two compounds in $rCa_v1.1AM$ and $hCa_v1.3AS$ is nearly identical, including the interaction between the tertiary amine and the phosphate groups of the two drugs (Figures 4B,C).

The structures of $rCa_v1.1$ and $hCa_v1.3$ bound to AMIO and SOF/MNI-1 thus collectively demonstrate, to our best knowledge, an unprecedented mechanism of pharmacodynamic DDI through direct and specific physical interaction of the involved drugs, and reveal the molecular basis for the potentiation of AMIO action on LTCCs by SOF/MNI-1.

Discussion

The stereochemistry of prodrug component of the HCV inhibitors determines their cardiac DDI with AMIO (Lagrutta et al., 2017). For example, no bradycardia is observed when MK-3682, which has opposite chirality at the amino acyl and phosphoryl groups compared to SOF, is combined with AMIO (Regan et al., 2016). To probe the molecular basis for the stereochemistry effect, we performed molecular docking simulation using $hCa_v1.3AS$ as the template. Top ranking poses were selected for further comparison. Docking models of SOF align well with the experimental structure, with the RMSD of the top pose and the experimental one smaller than 2.0 Å (Figure 5A) (Hartshorn et al., 2007; Su et al., 2019). Moreover, the high ranking poses of SOF can be superimposed, with the RMSD values to the top one all less than 2.5 Å (Figures 5B,C).

When MK-3682 was docked to AMIO-bound $Ca_v1.3$, the pyrimidinedione ring and other groups displayed rather flexible binding modes, resulting in a broader range of RMSD values of the four docking poses, all above 4 Å (Figure 5C). We used the molecular mechanics generalized Born surface area (MM/GBSA) method (Wang et al., 2019) to calculate the predicted free energies (ΔG_{bind}) for the binding of MK-3682 or SOF with $hCa_v1.3$. The average ΔG_{bind} values for the four docking poses of MK-3682 and SOF are −37.3 kcal/mol and −46.0 kcal/mol, respectively (Figure 5C). The larger RMSD and ΔG_{bind} values consistently suggest a less favored binding of MK-3682 with LTCCs, thereby affording additional evidence for the chiral specificity of the interaction between SOF/MNI-1 and AMIO.

DDIs are a cause for adverse drug reactions, mostly through pharmacodynamics, pharmacokinetics, and pharmaceutical incompatibility (Niu et al., 2019; Palleria et al., 2013). Direct physical interactions enabled by one of the drug targets has been rarely described. Our systematic structural analysis shows a direct physical, pharmacodynamic interaction of an antiviral and an antiarrhythmic reagent on the scaffold of a protein, which underlies the clinically relevant, potentially life-threatening DDI of the two drugs.

Limitation of the study:

The present study is heavily structure-oriented. Mutational analysis was hindered by serious rundown of $Ca_v1.2$ and $Ca_v1.3$ mutants during electrophysiological recordings. Although the

improved densities for MNI-1 and SOF in accordance with their increasing concentrations validate their binding poses (Figure 1E), these structures cannot reveal the dynamics or kinetics of the interactions between the drugs or with LTCCs. It is also unclear how SOF/MNI-1 gets access to the central cavity of LTCCs.

STAR★Methods

RESOURCE AVAILABILITY

Lead contact—Further information and requests for reagents may be directed and will be fulfilled by Nieng Yan (nyan@princeton.edu), the lead contact.

Materials availability—Plasmids generated in this study will be made available on request, but we may require a payment and/or a completed Materials Transfer Agreement if there is potential for commercial application.

Data and code availability

- Atomic coordinates of rCa$_v$1.1A, rCa$_v$1.1AM0.1, rCa$_v$1.1AM, hCa$_v$1.3A, hCa$_v$1.3S, and hCa$_v$1.3AS have been deposited in the Protein Data Bank (http://www.rcsb.org) and are publicly available as of the date of publication under the accession codes 8E56, 8E57, 8E58, 8E59, 8E5A, and 8E5B, respectively. The corresponding EM maps of rCa$_v$1.1A, rCa$_v$1.1AM0.1, rCa$_v$1.1AM, hCa$_v$1.3A, hCa$_v$1.3S, and hCa$_v$1.3AS have been deposited in the Electron Microscopy Data Bank (https://www.ebi.ac.uk/pdbe/emdb/), under the accession codes EMD-27904, EMD-27905, EMD-27906, EMD-27907, EMD-27908, and EMD-27909, respectively. These accession numbers are also listed in the key resources table. All other data is available from the corresponding authors upon reasonable request.
- This paper does not report original code.
- Any additional information required to reanalyze the data reported in this paper is available from the lead contact upon request.

EXPERIMENTAL MODEL AND SUBJECT DETAILS

Cell culture—All *E. coli* cells were cultured in LB medium (Sigma) at 37 °C. The BL21(DE3) strain was used to express β1 subunit, and HST08 strain (Stellar™, TaKaRa) was used to amplify plasmids.

HEK293F suspension cells (Thermo Fisher Scientific, R79007) were cultured in Freestyle 293 medium (Thermo Fisher Scientific) at 37 °C supplied with 5% CO_2 under 80% humidity.

HEK293 cells stably overexpressing human Ca$_v$1.2 channel complex and Kir2.3 inward rectifier K channel (Xia et al., 2004) were cultured in Dulbecco's modified Eagle Glutamax's medium (Invitrogen) with 10% fetal bovine serum (Invitrogen), 100 U/mL penicillin-streptomycin (Invitrogen), Geneticin (G418) (Invitrogen), Zeocin (Invitrogen), and Hygromycin B (Invitrogen) at 37 °C under a humidified atmosphere of 5% CO_2.

METHOD DETAILS

$Ca_V1.2$ calcium influx assay—HEK293 cells overexpressing human $Ca_V1.2$ channel and Kir2.3 channel were plated on 96-well plates at a density of 60,000 cells/well (Xia et al., 2004). Cells were maintained in culture (37 °C, 5% CO_2) overnight before use. On experiment day, cells were incubated with Codex ACTOne® dye (Codex Biosolution Inc.) formulated in PPB buffer containing 25 mM potassium (127 mM NaCl, 25 mM KCl, 0.005 mM $CaCl_2$, 1.7 mM $MgCl_2$, 10 mM HEPES 7.2) for 30 minute at room temperature, then test compounds were added for another 30-minute incubation at room temperature with a final volume of 100 μL. FDSS/μCell imaging platform simultaneously collected Ca^{2+} signals from 96-well plates, at a sampling rate of 16 Hz for 20 s as baseline, then a trigger buffer (119 mM NaCl, 25 mM KCl, 4 mM $CaCl_2$, 1.7 mM $MgCl_2$, 10 mM HEPES 7.2) was added using the dispenser of the FDSS/μCell instrument to generate Ca^{2+} transient for 40 s. The peak amplitude within the latter 40 s minus the average amplitude of the first 20 s is the final Ca^{2+} response of each well. Average response from wells treated with 0.1 μM Isradipine (reference Ca_v blocker, Carbosynth Ltd) was set as 100% inhibition (Rmax); and average response from wells treated with 0.1% DMSO was set as 0% inhibition (Rmin). Relative response of each well was calculated as follows:

$$\% \text{ inhibition} = 100 * (\text{Rmin} - \text{Response of each well}) \ / \ (\text{Rmin} - \text{Rmax}).$$

Modelling of the Ca^{2+} influx data is based on the reported equation that inhibition of two independent blockers is Total%=A%+B%-A%*B%, where A% and B% are the percent inhibition of two blocker alone (Jarvis and Thompson, 2013). This equation can be presented as Total%-A% = B%(1-A%). In this study, we defined “% total inhibition - % inhibition by Ca_v blockers alone” as the experimental MNI-1 inhibition with the Ca_v blocker as baseline (Y axis), and the calculation by two drugs alone “% Inhibition by MNI-1 alone * (1 - % inhibition by Ca_v blockers alone)” as the theoretical MNI-1 inhibition (X axis). If there is no interaction between tested compounds (nifedipine and MNI-1), a close to 1:1 linear fitting is predicted. Also shown in Figure 1D are deviations from this 1:1 linearity, expected if there is competition between two drugs at high concentrations as the case for co-applying verapamil and MNI-1. AMIO and MIN-1 show a synergistic interaction as the experimental values are much higher than the theoretical ones.

Transient expression of human $Ca_V1.3$ in HEK293F cells—Codon-optimized cDNAs of *CACNA1D* for $Ca_V1.3$-α1 (2,161 residues, Uniprot Q01668-1), *CACNA2D1* for α2δ-1 (1,103 residues, Uniprot P54289-1), and *CACNB3* for β3 (484 residues, Uniprot P54284-1) were synthesized (Wuxi Qinglan Biotech. Inc). Full-length $Ca_V1.3$-α1, α2δ-1, and β3 were subcloned into the pCAG vector, with tandem twin-strep and Flag tags at the amino (N) terminus for α1 subunits, and N-terminal Flag tag and C-terminal His tag for β3 subunit. When HEK293F cell density reached 1.5-2.0 * 10^6 cells/mL, a mixture of the expressing plasmids, including 0.75 mg α1, 0.6 mg α2δ-1 and 0.5 mg β3, together with 3 mg polyethylenimine (Polysciences) was added to the cell culture for transient expression of the human $Ca_V1.3$ complex.

Protein preparation—The endogenous $rCa_v1.1$ complex was purified following identical protocol as reported (Gao and Yan, 2021). For $hCa_v1.3$, seven liters of suspension HEK293F cells were harvested approximately 72 hours after transfection by centrifugation at 3,600 g for 10 min and resuspended in the lysis buffer containing 25 mM HEPES (pH 7.4), 150 mM NaCl, and the protease inhibitor cocktail containing 2.6 μg/mL aprotinin (VWR Life Science) and 1.4 μg/mL pepstatin (VWR Life Science). After sonication on ice, the suspension was supplemented with glyco-diosgenin (GDN, Anatrace) to a final concentration of 1% (w/v), *n*-dodecyl-β-D-maltopyranoside (DDM, Anatrace) to 0.2% (w/v), and cholesteryl hemisuccinate Tris salt (CHS, Anatrace) to 0.04% (w/v). After incubation at 4 °C overnight, the mixture was centrifuged at 35,000g for 30 min, and the supernatant was applied to anti-Flag M2 affinity resin (Sigma). The resin was rinsed with wash buffer (buffer A) containing 25 mM HEPES (pH 7.4), 150 mM NaCl, 2 mM $CaCl_2$, and 0.01% GDN. Eluted with buffer A plus 0.2 mg/mL Flag peptide (synthesized by GenScript), the eluent was concentrated using a 100 kDa cut-off Amicon (Millipore) and further purified through size-exclusion chromatography (SEC, Superose 6 10/300 GL, GE Healthcare) pre-equilibrated in buffer A. The peak fractions were pooled and concentrated.

To prepare Ca_v-drug complexes, concentrated proteins ($rCa_v1.1$ at ~5 mg/mL, and $hCa_v1.3$ at ~15 mg/mL) were incubated with drugs at 4 °C for 30 min before making cryo-grids.

$rCa_v1.1A$: Amiodarone (MedChemExpress) was added to $rCa_v1.1$ proteins at a final concentration of 100 μM.

$rCa_v1.1AM0.1$: Amiodarone and MNI-1 (provided by Merck & Co., Inc., Rahway, NJ, USA) were added together to $rCa_v1.1$ proteins both at 100 μM.

$rCa_v1.1AM$: $rCa_v1.1$ proteins in the presence of 100 μM amiodarone and 1 mM MNI-1.

$hCa_v1.3A$: $hCa_v1.3$ proteins in the presence of 140 μM amiodarone.

$hCa_v1.3S$: $hCa_v1.3$ proteins in the presence of 1.4 mM sofosbuvir (MedChemExpress).

$hCa_v1.3AS$: $hCa_v1.3$ proteins in the presence of 140 μM amiodarone and 1.4 mM sofosbuvir.

Cryo-sample preparation and data collection—Aliquots of 3.5 μL concentrated samples were loaded onto glow-discharged holey carbon grids (Quantifoil Au 300 mesh, R1.2/1.3 and Quantifoil Cu 300 mesh, R1.2/1.3), which were blotted for 6 s and plunge-frozen in liquid ethane cooled by liquid nitrogen using a Vitrobot MarK IV (Thermo Fisher) at 8 °C with 100% humidity. Grids were transferred to a Titan Krios electron microscope (Thermo Fisher) operating at 300 kV and equipped with a Gatan Gif Quantum energy filter (slit width 20 eV) and spherical aberration (Cs) image corrector. Micrographs were recorded using a K2 Summit counting camera (Gatan Company) in super-resolution mode with a nominal magnification of 105,000x, resulting in a calibrated pixel size of 0.557 Å. Each stack of 32 frames was exposed for 5.6 s, with an exposure time of 0.175 s per frame. The total dose for each stack was ~ 50 $e^{-}/Å^2$. SerialEM was used for fully automated data collection (Mastronarde, 2005). All 32 frames in each stack were aligned, summed, and dose

weighted using MotionCorr2 (Zheng et al., 2017) and 2-fold binned to a pixel size of 1.114 Å/pixel. The defocus values were set from −1.9 to −2.1 μm and estimated by Gctf (Zhang, 2016).

Image processing—A total of 1,677 (rCa$_v$1.1A), 1,794 (rCa$_v$1.1AM0.1), 2,013 (rCa$_v$1.1AM), 2,302 (hCa$_v$1.3A), 1,770 (hCa$_v$1.3S) and 2,032 (hCa$_v$1.3AS) cryo-EM micrographs were collected, and 831,227 (rCa$_v$1.1A), 688,386 (rCa$_v$1.1AM0.1), 1,014,749 (rCa$_v$1.1AM), 1,351,225 (hCa$_v$1.3A), 1,297,831 (hCa$_v$1.3S) and 1,288,216 (hCa$_v$1.3AS) particles were auto-picked by RELION-3.0 (Zivanov et al., 2018). Particle picking was performed using the selected 2D class of rabbit Ca$_v$1.1 as reference (Gao and Yan, 2021). All subsequent 2D and 3D classifications and refinements were performed using RELION-3.0.

Reference-free 2D classification were performed to remove ice spots, contaminants, and aggregates, yielding 777,536 (rCa$_v$1.1A), 581,605 (rCa$_v$1.1AM0.1), 911,176 (rCa$_v$1.1AM), 1,276,190 (hCa$_v$1.3A), 1,151,864 (hCa$_v$1.3S) and 1,121,237 (hCa$_v$1.3AS) particles. The particles were processed with a global search with K=1 to determine the initial orientation alignment parameters using bin2 particles. A published EM map of rabbit Ca$_v$1.1 (EMD-22426) low-pass filtered to 20 Å was used as an initial reference (Gao and Yan, 2021). The output of the 35–40 iterations was further applied to local angular search 3D classification with four classes. A total of 400,307 (rCa$_v$1.1A), 260,673 (rCa$_v$1.1AM0.1), 381,524 (rCa$_v$1.1AM), 516,088 (hCa$_v$1.3A), 407,272 (hCa$_v$1.3S) and 470,281 (hCa$_v$1.3AS) particles were selected by combining the good classes of the local angular search 3D classification. The particles were then re-extracted using a box size of 280 and pixel size of 1.114 Å. These particles yielded reconstructions at 3.0 Å (rCa$_v$1.1A), 3.1 Å (rCa$_v$1.1AM0.1), 3.6 Å (rCa$_v$1.1AM), 3.5 Å (hCa$_v$1.3A), 3.6 Å (hCa$_v$1.3S) and 4.0 Å (hCa$_v$1.3AS) after 3D auto-refinement with an adapted mask. Skip align 3D classification using bin1 particles and Bayesian polishing resulted in final reconstructions at 2.8 Å (rCa$_v$1.1A), 2.8 Å (rCa$_v$1.1AM0.1), 3.0 Å (rCa$_v$1.1AM), 3.1 Å (hCa$_v$1.3A), 3.3 Å (hCa$_v$1.3S) and 3.3 Å (hCa$_v$1.3AS) from 400,307 (rCa$_v$1.1A), 190,835 (rCa$_v$1.1AM0.1), 83,355 (rCa$_v$1.1AM), 86,836 (hCa$_v$1.3A), 73,092 (hCa$_v$1.3S) and 69,718 (hCa$_v$1.3AS) particles.

All 2D classification, 3D classification, and 3D auto-refinement were performed with RELION-3.0. Resolutions were estimated with the gold-standard Fourier shell correlation 0.143 criterion with high-resolution noise substitution (Chen et al., 2013; Rosenthal and Henderson, 2003).

Model building and refinement—The previously reported rCa$_v$1.1 structure (PDB: 5GJV) was used as starting model that was docked into the maps for rCa$_v$1.1-A/AM0.1/AM in Chimera (Pettersen et al., 2004), respectively. Model building of Ca$_v$1.3 was based on the reported structures of both Ca$_v$1.1 and Ca$_v$2.2. The starting model of Ca$_v$1.3 α1 subunit was built in SWISS-MODEL (Waterhouse et al., 2018) based on the structure of rCa$_v$1.1 (PDB: 5GJV), and those of α2δ-1 and β3 were based on the structure of Ca$_v$2.2 (PDB: 7MIY). The starting model of Ca$_v$1.3 was then manually docked into the 3.1 Å hCa$_v$1.3A 3D map in Chimera and manually adjusted in COOT (Emsley et al., 2010). For model building of the

hCa$_v$1.3S/AS, the coordinates for α1, α2δ-1 and β3 from Ca$_v$1.3A were docked into the 3.3 Å Ca$_v$1.3S/AS map separately and manually adjusted in COOT.

Additional lipids and ligands were manually built to fit into the corresponding densities in COOT. Models were manually adjusted in COOT, followed by refinement against the corresponding maps by the phenix.real_space_refine program in PHENIX (Adams et al., 2010) with secondary structure and geometry restraints. Statistics of 3D reconstructions and model refinement can be found in Table 1 and 2. All structure figures were prepared in PyMol (DeLano, 2002), UCSF Chimera (Pettersen et al., 2004) and ChimeraX (Goddard et al., 2018).

Molecular docking simulation—After removing SOF from hCa$_v$1.3AS structure, SOF and MK-3682 were separately docked using Schrödinger Suite 2018-1 (Schrödinger, Inc.) in the presence of AMIO. The initial 3D conformations of ligands were generated from their 2D structures using the LigPrep program (Sastry et al., 2013) with the OPLS3 force field (Harder et al., 2016). The protein structure was processed by Protein Preparation Wizard using the coordinates of hCa$_v$1.3AS as input. Molecular docking simulations were performed using extra-precision docking (Glide XP) within the Glide program.

QUANTIFICATION AND STATISTICAL ANALYSIS

The local resolution map was calculated using RELION-3.0 (Zivanov et al., 2018). Resolutions were estimated with the gold-standard Fourier shell correlation 0.143 criterion (Rosenthal and Henderson, 2003) with high-resolution noise substitution. Statistical analysis of Ca$_v$1.2 calcium influx assays was performed using Prism 9 (GraphPad Software, San Diego, CA, USA). Data represent mean ± SEM obtained from three independent experiments performed in quadruplicate.

Supplementary Material

Refer to Web version on PubMed Central for supplementary material.

Acknowledgements

We thank the cryo-EM facility at Princeton Imaging and Analysis Center operated by the Princeton Institute of Materials at Princeton University, which is supported in part by the Princeton Center for Complex Materials, a National Science Foundation Materials Research Science and Engineering Center (Grant No. DMR-2011750). The work was supported by grant from NIH (5R01GM130762 to N.Y. and R01DK125404 to Y.Y.).

References:

Adams PD, Afonine PV, Bunkóczi G, Chen VB, Davis IW, Echols N, Headd JJ, Hung LW, Kapral GJ, Grosse-Kunstleve RW, et al. (2010). PHENIX: a comprehensive Python-based system for macromolecular structure solution. Acta Crystallogr D Biol Crystallogr 66, 213–221. 10.1107/s0907444909052925. [PubMed: 20124702]

Afdhal N, Zeuzem S, Kwo P, Chojkier M, Gitlin N, Puoti M, Romero-Gomez M, Zarski JP, Agarwal K, Buggisch P, et al. (2014). Ledipasvir and sofosbuvir for untreated HCV genotype 1 infection. N Engl J Med 370, 1889–1898. 10.1056/NEJMoa1402454. [PubMed: 24725239]

Appleby TC, Perry JK, Murakami E, Barauskas O, Feng J, Cho A, Fox D 3rd, Wetmore DR, McGrath ME, Ray AS, et al. (2015). Viral replication. Structural basis for RNA replication by the hepatitis C virus polymerase. Science 347, 771–775. 10.1126/science.1259210. [PubMed: 25678663]

Back DJ, and Burger DM (2015). Interaction between amiodarone and sofosbuvir-based treatment for hepatitis C virus infection: potential mechanisms and lessons to be learned. Gastroenterology 149, 1315–1317. 10.1053/j.gastro.2015.09.031. [PubMed: 26416328]

Carbone E, and Lux HD (1984). A low voltage-activated, fully inactivating Ca channel in vertebrate sensory neurones. Nature 310, 501–502. 10.1038/310501a0. [PubMed: 6087159]

Chen S, McMullan G, Faruqi AR, Murshudov GN, Short JM, Scheres SH, and Henderson R (2013). High-resolution noise substitution to measure overfitting and validate resolution in 3D structure determination by single particle electron cryomicroscopy. Ultramicroscopy 135, 24–35. 10.1016/j.ultramic.2013.06.004. [PubMed: 23872039]

DeLano WL (2002). The PyMOL Molecular Graphics System. http://www.pymol.org.

Dolphin AC (2006). A short history of voltage-gated calcium channels. Br J Pharmacol 147 Suppl 1, S56–62. 10.1038/sj.bjp.0706442.

Emsley P, Lohkamp B, Scott WG, and Cowtan K (2010). Features and development of Coot. Acta Crystallogr D Biol Crystallogr 66, 486–501. 10.1107/s0907444910007493. [PubMed: 20383002]

Ertel EA, Campbell KP, Harpold MM, Hofmann F, Mori Y, Perez-Reyes E, Schwartz A, Snutch TP, Tanabe T, Birnbaumer L, et al. (2000). Nomenclature of voltage-gated calcium channels. Neuron 25, 533–535. 10.1016/s0896-6273(00)81057-0. [PubMed: 10774722]

Gao S, and Yan N (2021). Structural Basis of the Modulation of the Voltage-Gated Calcium Ion Channel Ca(v)1.1 by Dihydropyridine Compounds**. Angewandte Chemie-International Edition 60, 3131–3137. 10.1002/anie.202011793. [PubMed: 33125829]

Gao S, Yao X, and Yan N (2021). Structure of human Cav2.2 channel blocked by the painkiller ziconotide. Nature 596, 143–147. 10.1038/s41586-021-03699-6. [PubMed: 34234349]

Goddard TD, Huang CC, Meng EC, Pettersen EF, Couch GS, Morris JH, and Ferrin TE (2018). UCSF ChimeraX: Meeting modern challenges in visualization and analysis. Protein Sci 27, 14–25. 10.1002/pro.3235. [PubMed: 28710774]

Harder E, Damm W, Maple J, Wu C, Reboul M, Xiang JY, Wang L, Lupyan D, Dahlgren MK, Knight JL, et al. (2016). OPLS3: A Force Field Providing Broad Coverage of Drug-like Small Molecules and Proteins. J Chem Theory Comput 12, 281–296. 10.1021/acs.jctc.5b00864. [PubMed: 26584231]

Hartshorn MJ, Verdonk ML, Chessari G, Brewerton SC, Mooij WT, Mortenson PN, and Murray CW (2007). Diverse, high-quality test set for the validation of protein-ligand docking performance. J Med Chem 50, 726–741. 10.1021/jm061277y. [PubMed: 17300160]

Jacobson IM, Gordon SC, Kowdley KV, Yoshida EM, Rodriguez-Torres M, Sulkowski MS, Shiffman ML, Lawitz E, Everson G, Bennett M, et al. (2013). Sofosbuvir for hepatitis C genotype 2 or 3 in patients without treatment options. N Engl J Med 368, 1867–1877. 10.1056/NEJMoa1214854. [PubMed: 23607593]

Jarvis GE, and Thompson AJ (2013). A golden approach to ion channel inhibition. Trends Pharmacol Sci 34, 481–488. 10.1016/j.tips.2013.07.004. [PubMed: 23972927]

Kodama I, Kamiya K, and Toyama J (1997). Cellular electropharmacology of amiodarone. Cardiovasc Res 35, 13–29. 10.1016/s0008-6363(97)00114-4. [PubMed: 9302343]

Kohlhardt M, and Fleckenstein A (1977). Inhibition of the slow inward current by nifedipine in mammalian ventricular myocardium. Naunyn-Schmiedeberg's archives of pharmacology 298, 267–272. [PubMed: 895901]

Lagrutta A, Regan CP, Zeng H, Imredy JP, Koeplinger K, Morissette P, Liu L, Wollenberg G, Brynczka C, Lebrón J, et al. (2017). Cardiac drug-drug interaction between HCV-NS5B pronucleotide inhibitors and amiodarone is determined by their specific diastereochemistry. Sci Rep 7, 44820. 10.1038/srep44820. [PubMed: 28327633]

Lagrutta A, Zeng H, Imredy J, Balasubramanian B, Dech S, Lis E, Wang J, Zhai J, DeGeorge J, and Sannajust F (2016). Interaction between amiodarone and hepatitis-C virus nucleotide inhibitors in human induced pluripotent stem cell-derived cardiomyocytes and HEK-293 Cav1.2

over-expressing cells. Toxicol Appl Pharmacol 308, 66–76. 10.1016/j.taap.2016.08.006. [PubMed: 27520758]

Lawitz E, Mangia A, Wyles D, Rodriguez-Torres M, Hassanein T, Gordon SC, Schultz M, Davis MN, Kayali Z, Reddy KR, et al. (2013). Sofosbuvir for previously untreated chronic hepatitis C infection. N Engl J Med 368, 1878–1887. 10.1056/NEJMoa1214853. [PubMed: 23607594]

Lubic SP, Nguyen KP, Dave B, and Giacomini JC (1994). Antiarrhythmic agent amiodarone possesses calcium channel blocker properties. J Cardiovasc Pharmacol 24, 707–714. 10.1097/00005344-199424050-00004. [PubMed: 7532747]

Mangia A, Milligan S, Khalili M, Fagiuoli S, Shafran SD, Carrat F, Ouzan D, Papatheodoridis G, Ramji A, Borgia SM, et al. (2020). Global real-world evidence of sofosbuvir/velpatasvir as simple, effective HCV treatment: Analysis of 5552 patients from 12 cohorts. Liver Int 40, 1841–1852. 10.1111/liv.14537. [PubMed: 32449966]

Mastronarde DN (2005). Automated electron microscope tomography using robust prediction of specimen movements. J Struct Biol 152, 36–51. 10.1016/j.jsb.2005.07.007. [PubMed: 16182563]

Millard DC, Strock CJ, Carlson CB, Aoyama N, Juhasz K, Goetze TA, Stoelzle-Feix S, Becker N, Fertig N, January CT, et al. (2016). Identification of Drug-Drug Interactions In Vitro: A Case Study Evaluating the Effects of Sofosbuvir and Amiodarone on hiPSC-Derived Cardiomyocytes. Toxicol Sci 154, 174–182. 10.1093/toxsci/kfw153. [PubMed: 27503387]

Niu J, Straubinger RM, and Mager DE (2019). Pharmacodynamic Drug-Drug Interactions. Clin Pharmacol Ther 105, 1395–1406. 10.1002/cpt.1434. [PubMed: 30912119]

Nokin P, Clinet M, Swillens S, Delisee C, Meysmans L, and Chatelain P (1986). Allosteric modulation of [3H]nitrendipine binding to cardiac and cerebral cortex membranes by amiodarone. J Cardiovasc Pharmacol 8, 1051–1057. 10.1097/00005344-198609000-00025. [PubMed: 2429079]

Nowycky MC, Fox AP, and Tsien RW (1985). Three types of neuronal calcium channel with different calcium agonist sensitivity. Nature 316, 440–443. 10.1038/316440a0. [PubMed: 2410796]

Palleria C, Di Paolo A, Giofrè C, Caglioti C, Leuzzi G, Siniscalchi A, De Sarro G, and Gallelli L (2013). Pharmacokinetic drug-drug interaction and their implication in clinical management. J Res Med Sci 18, 601–610. [PubMed: 24516494]

Pettersen EF, Goddard TD, Huang CC, Couch GS, Greenblatt DM, Meng EC, and Ferrin TE (2004). UCSF Chimera--a visualization system for exploratory research and analysis. J Comput Chem 25, 1605–1612. 10.1002/jcc.20084. [PubMed: 15264254]

Regan CP, Morissette P, Regan HK, Travis JJ, Gerenser P, Wen J, Fitzgerald K, Gruver S, DeGeorge JJ, and Sannajust FJ (2016). Assessment of the clinical cardiac drug-drug interaction associated with the combination of hepatitis C virus nucleotide inhibitors and amiodarone in guinea pigs and rhesus monkeys. Hepatology 64, 1430–1441. 10.1002/hep.28752. [PubMed: 27474787]

Rosenthal PB, and Henderson R (2003). Optimal determination of particle orientation, absolute hand, and contrast loss in single-particle electron cryomicroscopy. J Mol Biol 333, 721–745. DOI 10.1016/j.jmb.2003.07.013. [PubMed: 14568533]

Roy D, Talajic M, Dorian P, Connolly S, Eisenberg MJ, Green M, Kus T, Lambert J, Dubuc M, Gagne P, et al. (2000). Amiodarone to prevent recurrence of atrial fibrillation. Canadian Trial of Atrial Fibrillation Investigators. N Engl J Med 342, 913–920. 10.1056/NEJM200003303421302. [PubMed: 10738049]

Sastry GM, Adzhigirey M, Day T, Annabhimoju R, and Sherman W (2013). Protein and ligand preparation: parameters, protocols, and influence on virtual screening enrichments. J Comput Aided Mol Des 27, 221–234. 10.1007/s10822-013-9644-8. [PubMed: 23579614]

Stedman C (2014). Sofosbuvir, a NS5B polymerase inhibitor in the treatment of hepatitis C: a review of its clinical potential. Therap Adv Gastroenterol 7, 131–140. 10.1177/1756283X13515825.

Su M, Yang Q, Du Y, Feng G, Liu Z, Li Y, and Wang R (2019). Comparative Assessment of Scoring Functions: The CASF-2016 Update. J Chem Inf Model 59, 895–913. 10.1021/acs.jcim.8b00545. [PubMed: 30481020]

Tanabe T, Takeshima H, Mikami A, Flockerzi V, Takahashi H, Kangawa K, Kojima M, Matsuo H, Hirose T, and Numa S (1987). Primary structure of the receptor for calcium channel blockers from skeletal muscle. Nature 328, 313–318. 10.1038/328313a0. [PubMed: 3037387]

Wang E, Sun H, Wang J, Wang Z, Liu H, Zhang JZH, and Hou T (2019). End-Point Binding Free Energy Calculation with MM/PBSA and MM/GBSA: Strategies and Applications in Drug Design. Chem Rev 119, 9478–9508. 10.1021/acs.chemrev.9b00055. [PubMed: 31244000]

Waterhouse A, Bertoni M, Bienert S, Studer G, Tauriello G, Gumienny R, Heer FT, de Beer TAP, Rempfer C, Bordoli L, et al. (2018). SWISS-MODEL: homology modelling of protein structures and complexes. Nucleic Acids Res 46, W296–w303. 10.1093/nar/gky427. [PubMed: 29788355]

Wu J, Yan Z, Li Z, Qian X, Lu S, Dong M, Zhou Q, and Yan N (2016). Structure of the voltage-gated calcium channel Ca(v)1.1 at 3.6 A resolution. Nature 537, 191–196. 10.1038/nature19321. [PubMed: 27580036]

Wu J, Yan Z, Li Z, Yan C, Lu S, Dong M, and Yan N (2015). Structure of the voltage-gated calcium channel Cav1.1 complex. Science 350, aad2395. 10.1126/science.aad2395. [PubMed: 26680202]

Xia M, Imredy JP, Koblan KS, Bennett P, and Connolly TM (2004). State-dependent inhibition of L-type calcium channels: cell-based assay in high-throughput format. Anal Biochem 327, 74–81. 10.1016/j.ab.2004.01.003. [PubMed: 15033513]

Yao X, Gao S, and Yan N (2022). Structural basis for pore blockade of human voltage-gated calcium channel Ca(v)1.3 by motion sickness drug cinnarizine. Cell Res. 10.1038/s41422-022-00663-5.

Zamponi GW, Striessnig J, Koschak A, and Dolphin AC (2015). The Physiology, Pathology, and Pharmacology of Voltage-Gated Calcium Channels and Their Future Therapeutic Potential. Pharmacol Rev 67, 821–870. 10.1124/pr.114.009654. [PubMed: 26362469]

Zhang K (2016). Gctf: Real-time CTF determination and correction. J Struct Biol 193, 1–12. 10.1016/j.jsb.2015.11.003. [PubMed: 26592709]

Zhao Y, Huang G, Wu J, Wu Q, Gao S, Yan Z, Lei J, and Yan N (2019). Molecular Basis for Ligand Modulation of a Mammalian Voltage-Gated Ca(2+) Channel. Cell 177, 1495–1506 e1412. 10.1016/j.cell.2019.04.043. [PubMed: 31150622]

Zheng SQ, Palovcak E, Armache JP, Verba KA, Cheng Y, and Agard DA (2017). MotionCor2: anisotropic correction of beam-induced motion for improved cryo-electron microscopy. Nat Methods 14, 331–332. 10.1038/nmeth.4193. [PubMed: 28250466]

Zivanov J, Nakane T, Forsberg BO, Kimanius D, Hagen WJ, Lindahl E, and Scheres SH (2018). New tools for automated high-resolution cryo-EM structure determination in RELION-3. Elife 7. 10.7554/eLife.42166.

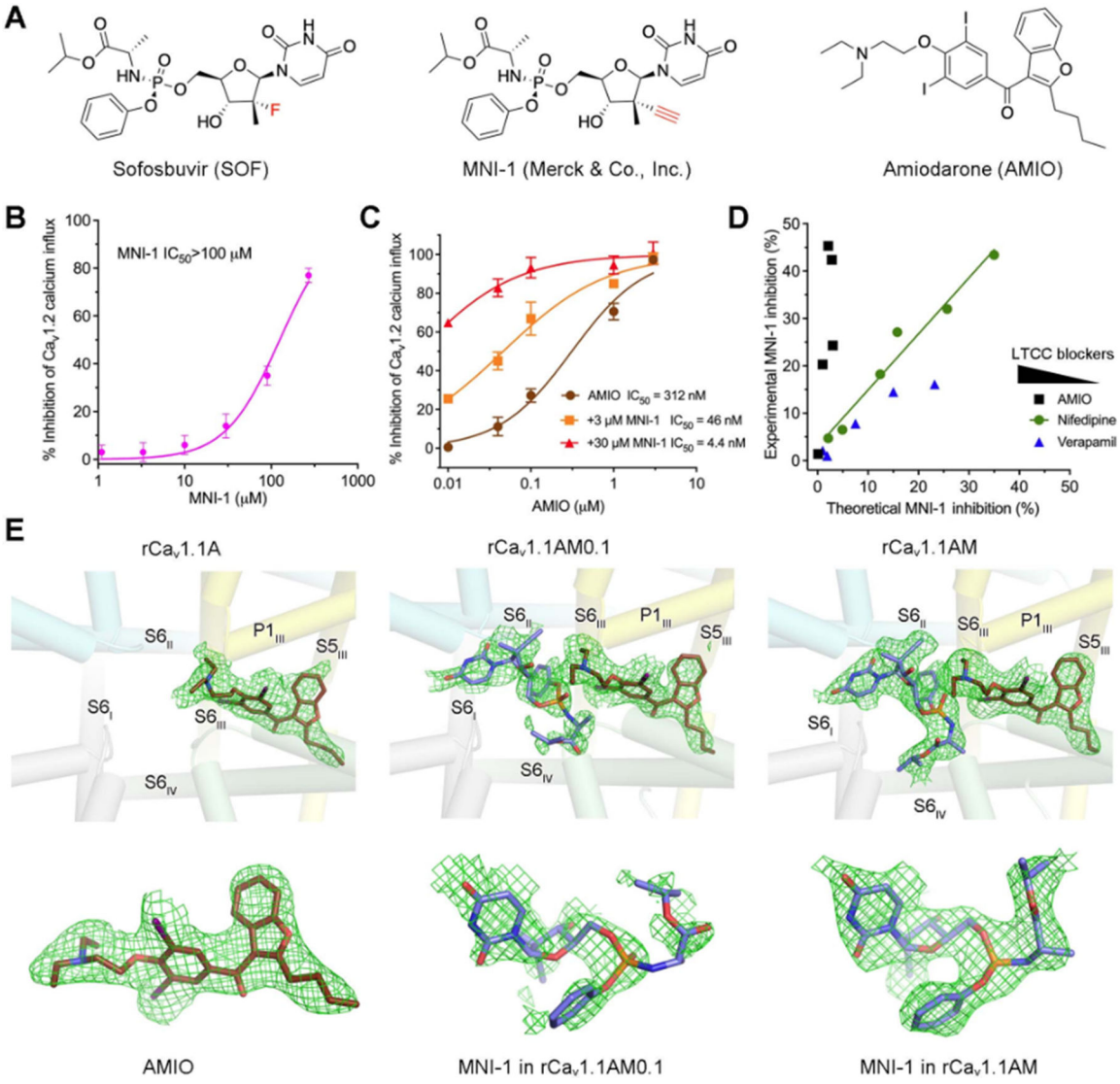

Figure 1 |. Cryo-EM analysis of rabbit $Ca_V1.1$ in the presence of AMIO and MNI-1.

(**A**) Chemical structures of sofosbuvir (SOF), MNI-1, and amiodarone (AMIO). (**B**) MNI-1 exhibits incomplete inhibition of $Ca_V1.2$ when applied at high concentrations. IC_{50} of MNI-1 was measured by $Ca_V1.2$ calcium influx assay. Values were normalized to the average response by 0.1 μM isradipine (as 100% inhibition). IC_{50} curves of all the figures were generated by Graphpad Prism 9. Points represent mean ± SEM obtained from at least three independent experiments performed in quadruplicate. (**C**) Synergistic effect of AMIO on MNI-1. IC_{50} values were calculated using MNI-1 as baseline. (**D**) Modeling of pharmacodynamic effects of LTCC blockers on MNI-1. This figure was plotted from a batch of IC_{50} experiment measuring LTCC blockers supplemented with 3 μM MNI-1 (AMIO), or 90 μM MNI-1 (nifedipine and verapamil). Please refer to STAR★Methods for detailed explanation of the modeling. The concentrations of LTCC blockers decrease from left to right. (**E**) EM densities of the bound ligands. *Top*: The ligand densities in the pore domain (PD) of rabbit $Ca_V1.1$ in the presence of the indicated chemicals. r$Ca_V1.1$A: rabbit $Ca_V1.1$ implemented with 0.1 mM AMIO; r$Ca_V1.1$AM0.1: with 0.1 mM AMIO and 0.1 mM MNI-1;

rCa$_v$1.1AM: with 0.1 mM AMIO and 1 mM MNI-1. The domain coloured PD is shown as semi-transparent cylindrical cartoon. *Bottom*: Enlarged views of the EM densities for the indicated ligands. All the densities, shown as green meshes, are contoured at 4 σ. All structure figures are prepared in PyMol (DeLano, 2002). See also Figures S1, S2.

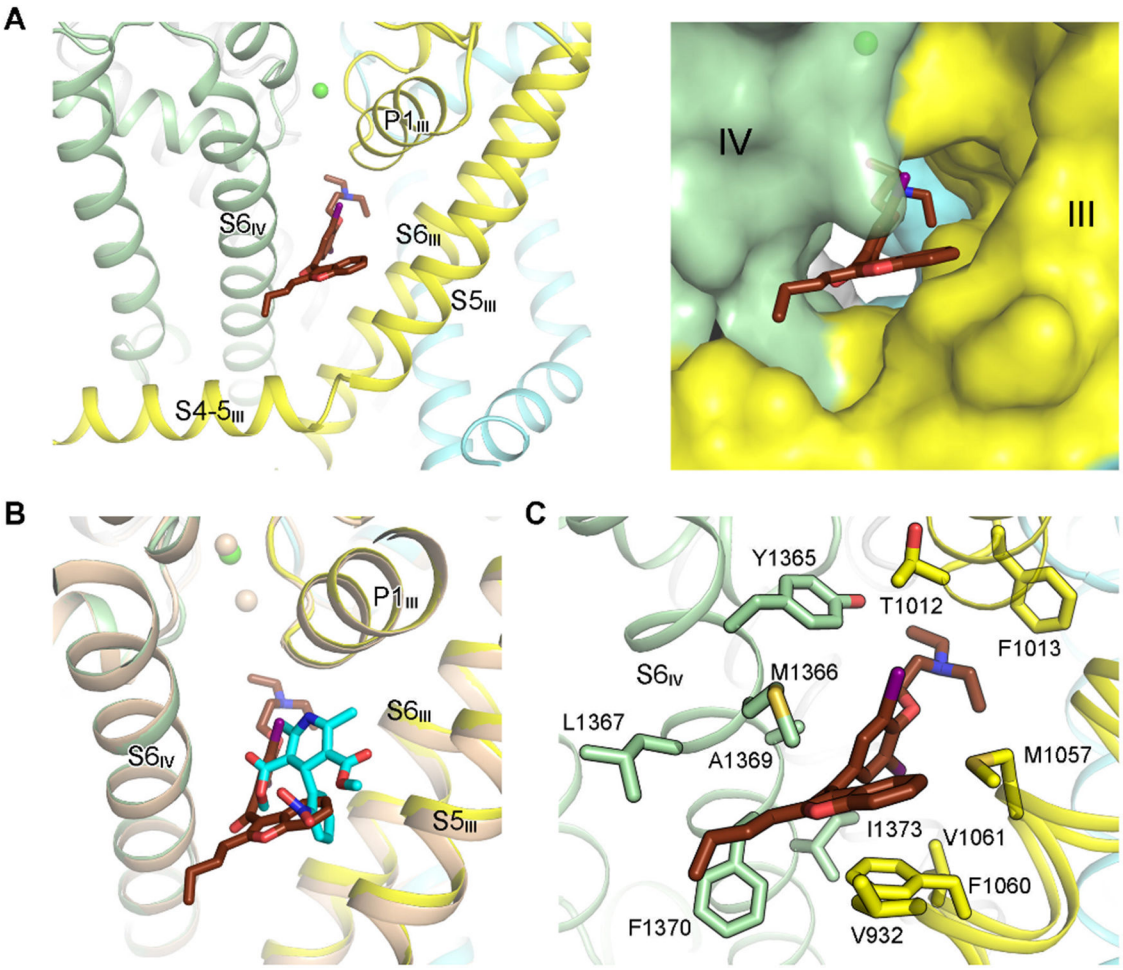

Figure 2 |. Coordination of AMIO in rCa$_v$1.1.

(**A**) AMIO inserts into the fenestration on the interface of repeats III and IV (the III-IV fenestration). The PD of rCa$_v$1.1A is shown as ribbon cartoon (*left*) or semi-transparent surface (*right*) to highlight the binding pocket for AMIO. (**B**) AMIO occupies the same binding site as the DHP compounds. Structures of the α1 subunit of rCa$_v$1.1A and nifedipine (cyan sticks)-bound rCa$_v$1.1 (colored wheat, PDB code: 6JP5) can be superimposed with RMSD of 0.57 Å over 970 aligned Cα atoms. (**C**) AMIO is coordinated exclusively through van der Waals contacts. AMIO and the surrounding residues are shown as sticks. See also Figure S2.

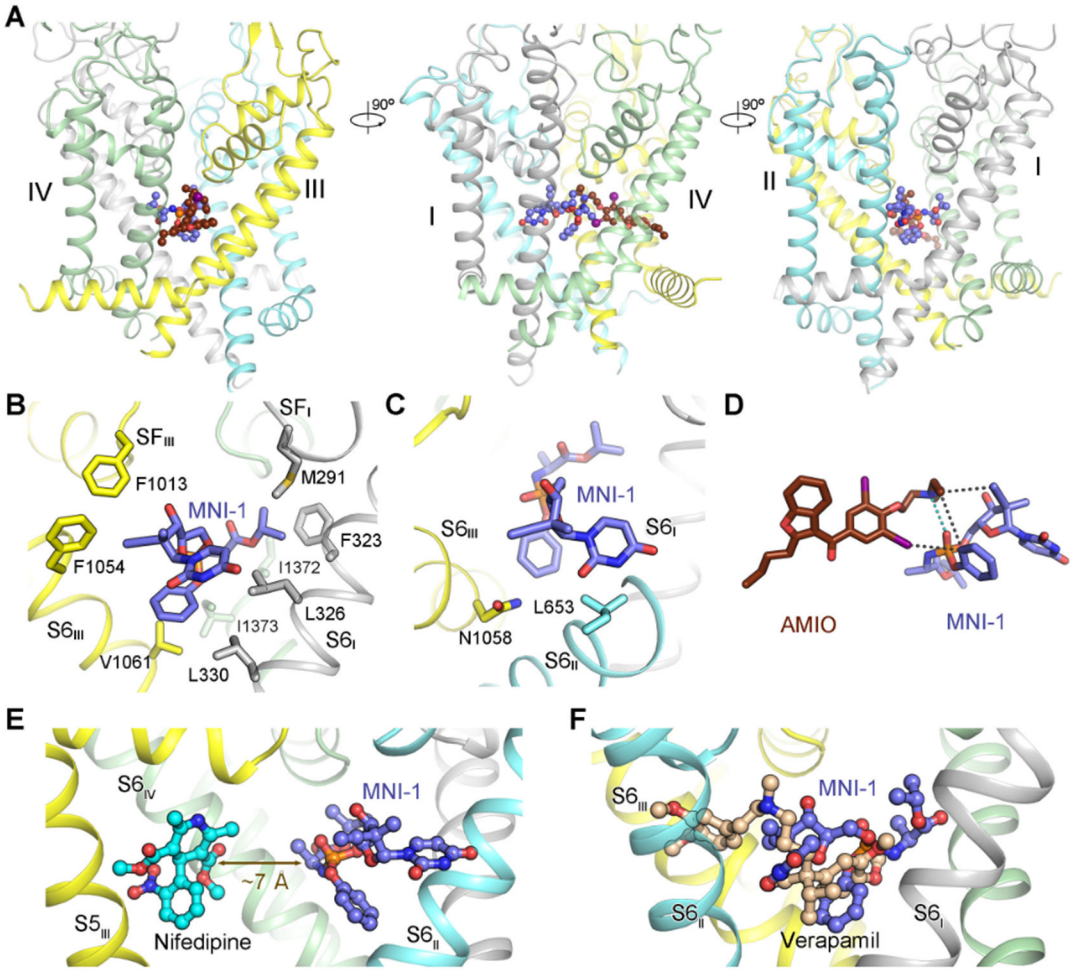

Figure 3 |. Direct drug-drug interaction (DDI) of AMIO and MNI-1 on rCa$_v$1.1.

(**A**) In the presence of AMIO, MNI-1 is accommodated in the central cavity of the PD. Three perpendicular side views of the PD are shown. AMIO and MNI-1 are shown as brown and purple ball-and-sticks, respectively. (**B**) The amphiphilic MNI-1 molecule is placed in a highly hydrophobic environment in rCa$_v$1.1. The MNI-1 coordinating residues, which are all hydrophobic, are shown as sticks. Repeat II and AMIO are omitted for visual clarity. (**C**) Less favored interactions between MNI-1 and rCa$_v$1.1 pore residues. Leu653 and Asn1058 are adjacent to polar and hydrophobic groups of MNI-1, respectively. (**D**) Direct interaction of AMIO and MNI-1. The polar interaction between the tertiary amine group in AMIO and the phosphate group in MNI-1 is indicated by cyan, dashed lines. The hydrophobic contacts between the two compounds are indicated by black, dashed lines. (**E**) Nifedipine does not interact with MNI-1 in rCa$_v$1.1. When the structure of nifedipine-bound rCa$_v$1.1 (PDB code: 6JP5) is overlaid with that of rCa$_v$1.1AM, the shortest distance between nifedipine and MNI-1 is ~ 7 Å, beyond the range for direction interactions. As the two structures are nearly identical, the protein scaffold of nifedipine-bound rCa$_v$1.1 is not shown. S6$_{III}$ and AMIO in rCa$_v$1.1AM are also omitted for clarity. (**F**) Overlapped binding poses of verapamil and MNI-1 explain their competition for binding to LTCCs. Verapamil-bound rCa$_v$1.1 structure

(PDB code: 6JPA) is used for comparison with $rCa_v1.1$AM, but only the ligand is shown. See also Figure S3.

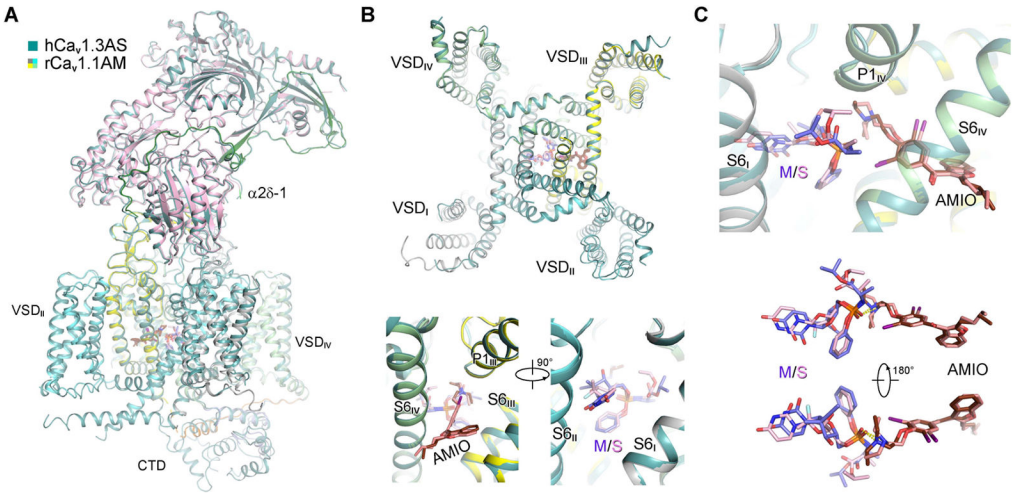

Figure 4 |. AMIO and SOF interact within human $Ca_V1.3$ ($hCa_V1.3$).

(**A**) The overall structure of $hCa_V1.3$ bound to AMIO and SOF ($hCa_V1.3AS$) is identical to that of $rCa_V1.1AM$. The two structures can be superimposed with an RMSD of 0.66 Å for 1782 Cα atoms in the α1 and α2δ-1 subunits. $rCa_V1.1AM$ is domain colored and $hCa_V1.3AS$ is colored dark green. (**B**) SOF and MNI-1 share identical binding pose in the presence of AMIO. *Top*: A cytosolic view of superimposed α1 subunits from $hCa_V1.3AS$ and $rCa_V1.1AM$. *Bottom*: Two opposite side views of superimposed α1 subunits from the two structures. (**C**) Direct interaction of SOF and AMIO within $hCa_V1.3AS$. SOF (pink) and MNI-1 (light purple), with similar chemical structures, interact with AMIO in the same way within the PD of LTCCs. See also Figures S4, S5.

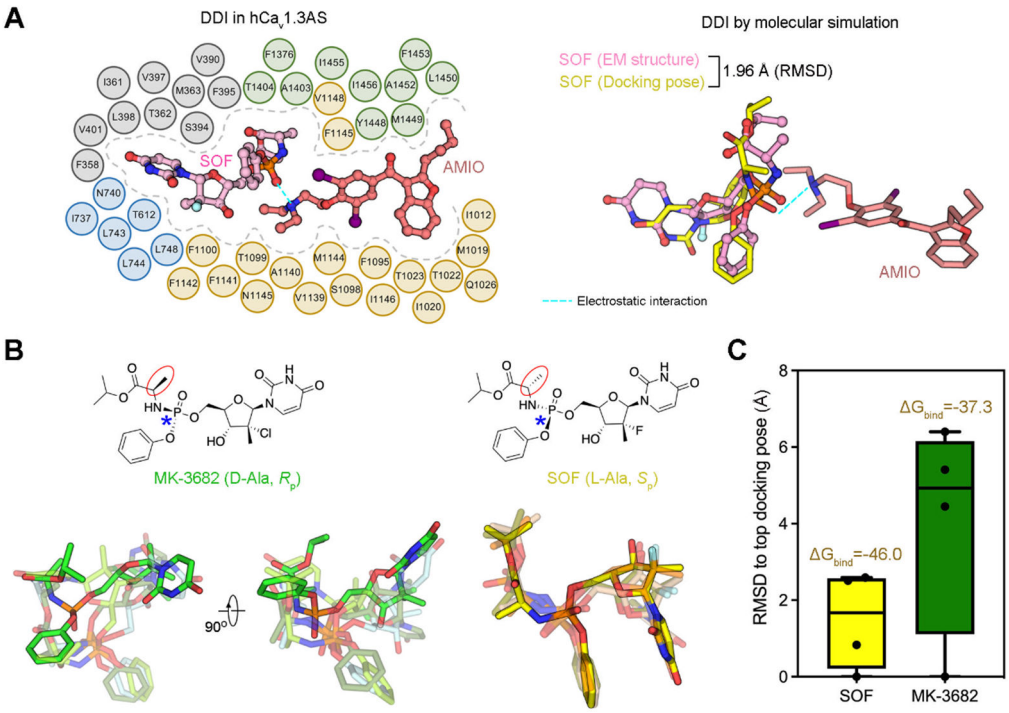

Figure 5 |. Chiral specificity of SOF for interaction with AMIO.

(**A**) Molecular docking simulation of the interaction between SOF and AMIO. *Left*: Schematic illustration of the association of AMIO and SOF with $hCa_V1.3AS$. Residues within 4 Å from either drug are shown and domain colored. *Right*: Molecular docking simulation is consistent with the cryo-EM structure. Interactions were simulated using $hCa_V1.3AS$ (without SOF) as the template. Shown in this figure are representative docking poses generated by Schrödinger software. The overall RMSD of the top ranking docking pose of SOF (yellow sticks) and the experimental one (pink ball-and-sticks) is < 2 Å, indicating high consistency (Hartshorn et al., 2007; Su et al., 2019). Importantly, the electrostatic interaction between the phosphate of SOF and the tertiary amine of AMIO, indicated by cyan dashes, is preserved in the simulation. (**B**) MK-3682, which has opposite chirality at the amino acyl and phosphoryl groups compared to SOF, displays variable binding poses in the molecular docking simulation. The stereochemical properties are labeled in parentheses below the chemical structures. L/D-Ala and S/R_P indicate the chirality of the amino acyl group (red cycles) and the phosphoryl group (blue asterisks), respectively. Four docking models are shown for MK-3682 (*left and middle*) and SOF (*right*). For visuality, the top and other docking poses are shown as opaque and transparent sticks, respectively. Compared to those of SOF, which are relatively well aligned, the docking poses of MK-3682 vary substantially. (**C**) Less favored binding of MK-3682 to LTCC in the presence of AMIO. MK-3682 shows more diverse docking poses, manifested by the larger and broader RMSD values of the top docking poses. The average binding free energy ΔG_{bind} (kcal/mol) of the top four docking poses for SOF (yellow) and MK-3682 (green), shown on the top of RMSD columns, was calculated with Prime MM-GBSA.

Table 1 |

Statistics for data collection and structural refinement of $rCa_v1.1$ structures. See also Figure S2.

	$rCa_v1.1$A (EMD-27904) (PDB 8E56)	**$rCa_v1.1$AM0.1 (EMD-27905) (PDB 8E57)**	**$rCa_v1.1$AM (EMD-27906) (PDB 8E58)**
Data collection and processing			
Magnification	105,000	105,000	105,000
Voltage (kV)	300	300	300
Electron dose (e-/Å^2)	50	50	50
Defocus range (μm)	−2.1~−1.9	−2.1~−1.9	−2.1~−1.9
Pixel size (Å)	1.114	1.114	1.114
Symmetry	C1	C1	C1
Initial particle images (no.)	831,227	688,386	1,014,749
Final particle images (no.)	400,307	190,835	83,355
Map resolution (Å)	2.8	2.8	3.0
FSC threshold	0.143	0.143	0.143
Refinement			
Initial model used (PDB code)	5GJV	5GJV	5GJV
Model resolution (Å)	2.9	3.0	3.1
FSC threshold	0.5	0.5	0.5
Map sharpening *B* factor (Å^2)	−67	−57	−65
Model composition			
Non-hydrogen atoms	18,461	18,449	18,449
Protein residues	2247	2247	2247
Ligands	28	28	28
B factors (Å^2)			
Protein	68.25	73.00	82.9
Ligand	127.27	102.15	99.8
R.m.s deviations			
Bond lengths (Å)	0.003	0.003	0.005
Bond angles (°)	0.555	0.518	0.620
Validation			
MolProbity score	1.78	1.61	1.78
Clashscore	7.60	5.90	7.37
Poor rotamers (%)	1.06	0.66	0.91
Ramachandran plot			
Favored (%)	95.07	95.84	94.48
Allowed (%)	4.93	4.16	5.43
Disallowed (%)	0.00	0.00	0.09

Table 2.

Statistics for data collection and structural refinement of $hCa_V1.3$ structures. See also Figure S4.

	$hCa_V1.3A$ (EMD-27907) (PDB 8E59)	**$hCa_V1.3S$ (EMD-27908) (PDB 8E5A)**	**$hCa_V1.3AS$ (EMD-27909) (PDB 8E5B)**
Data collection and processing			
Magnification	105,000	105,000	105,000
Voltage (kV)	300	300	300
Electron dose (e-/Å^2)	50	50	50
Defocus range (μm)	−2.1~−1.9	−2.1~−1.9	−2.1~−1.9
Pixel size (Å)	1.114	1.114	1.114
Symmetry	C1	C1	C1
Initial particle images (no.)	1,351,225	1,297,831	1,288,216
Final particle images (no.)	86,836	73,092	69,718
Map resolution (Å)	3.1	3.3	3.3
FSC threshold	0.143	0.143	0.143
Refinement			
Initial model used (PDB code)	5GJV, 7MIY	$hCa_V1.3A$	$hCa_V1.3A$
Model resolution (Å)	3.2	3.4	3.5
FSC threshold	0.5	0.5	0.5
Map sharpening *B* factor (Å^2)	−74	−96	−76
Model composition			
Non-hydrogen atoms	20311	20259	20312
Protein residues	2502	2502	2502
Ligands	19	17	18
B factors (Å^2)			
Protein	56.14	65.35	50.29
Ligand	83.29	102.35	71.99
R.m.s deviations			
Bond lengths (Å)	0.002	0.003	0.002
Bond angles (°)	0.485	0.661	0.515
Validation			
MolProbity score	1.72	2.08	1.73
Clashscore	6.70	10.00	7.18
Poor rotamers (%)	0.54	1.86	0.36
Ramachandran plot			
Favored (%)	94.86	94.82	95.15
Allowed (%)	5.10	4.98	4.81
Disallowed (%)	0.04	0.20	0.04

Key Resources Table

REAGENT or RESOURCE	SOURCE	IDENTIFIER
Bacterial and virus strains		
E. coli BL21(DE3)	Novagen	Cat# 69387-1
E. coli HST08 (Stellar™)	TaKaRa	Cat# 636766
Biological samples		
Rabbit muscle tissue	Pel-Freez	Cat# 41225 -2
Chemicals, peptides, and recombinant proteins		
Amiodarone	MedChemExpress	Cat# HY-14188
MNI-1	Merck & Co., Inc., Kenilworth, NJ, USA	N/A
Sofosbuvir	MedChemExpress	Cat# HY-15005
Isradipine	Carbosynth Ltd	Cat# 12-35-21-00
n-Dodecyl-β-D-Maltoside (DDM)	Anatrace	Cat# D310S
Glyco-diosgenin (GDN)	Anatrace	Cat# GDN101
Cholesteryl hemisuccinate Tris salt (CHS)	Anatrace	Cat# CH210
Aprotinin	VWR Life Science	Cat# 97062-754
Pepstatin	VWR Life Science	Cat# 97064-248
anti-Flag M2 affinity gel	MilliporeSigma	Cat# A2220
Flag peptide	GenScript	Cat# RP10586-1
Glutathione Sepharose® 4B	MilliporeSigma	Cat# GE17-0756-05
Dulbecco's modified Eagle Glutamax's medium	Invitrogen	Cat# 10566-016
Freestyle 293 medium	Thermo Fisher Scientific	Cat# 12338018
Fetal bovine serum (influx assay)	Invitrogen	Cat# 10082-139
Fetal Bovine Serum (protein expression)	Thermo Fisher Scientific	Cat# 10437028
LB medium	Sigma	Cat# L3522
Penicillin-streptomycin (100 U/mL)	Invitrogen	Cat# 15140-148
Geneticin (G418)	Invitrogen	Cat# 10131-035
Zeocin	Invitrogen	Cat# R250-01
Hygromycin B	Invitrogen	Cat# 10687-010
Polyethylenimine (PEI)	Polysciences	Cat# 24765-1
Codex ACTOne® dye	Codex Biosolution Inc.	Cat#: CB-80599-301
Superose 6™ Increase 10/300 GL	GE Healthcare	Cat# 29-0915-96
Deposited data		
Coordinates of rCa$_v$1.1A	This paper	PDB: 8E56
Coordinates of rCa$_v$1.1AM0.1	This paper	PDB: 8E57
Coordinates of rCa$_v$1.1AM	This paper	PDB: 8E58
Coordinates of hCa$_v$1.3A	This paper	PDB: 8E59
Coordinates of hCa$_v$1.3S	This paper	PDB: 8E5A

REAGENT or RESOURCE	SOURCE	IDENTIFIER
Coordinates of hCa$_v$1.3AS	This paper	PDB: 8E5B
Cryo-EM map of rCa$_v$1.1A	This paper	EMDB: EMD-27904
Cryo-EM map of rCa$_v$1.1AM0.1	This paper	EMDB: EMD-27905
Cryo-EM map of rCa$_v$1.1AM	This paper	EMDB: EMD-27906
Cryo-EM map of hCa$_v$1.3A	This paper	EMDB: EMD-27907
Cryo-EM map of hCa$_v$1.3S	This paper	EMDB: EMD-27908
Cryo-EM map of hCa$_v$1.3AS	This paper	EMDB: EMD-27909
Experimental models: Cell lines		
HEK293F cells	Thermo Fisher Scientific	Cat# R79007
HEK293 cells stably overexpressing human Ca$_v$1.2 channel complex and Kir2.3	(Xia et al., 2004)	N/A
Recombinant DNA		
Codon-optimized human Ca$_v$1.3-α1 cloned into a modified pCAG vector with tandem twin-strep and Flag tags at the amino (N) terminus	This paper	N/A
Codon-optimized human α2δ-1 subunit cloned into a modified pCAG vector	This paper	N/A
Codon-optimized human β3 subunit cloned into a modified pCAG vector with N-terminal Flag tag and C-terminal His$_{10}$ tag	This paper	N/A
Software and algorithms		
PyMOL	The PyMOL Molecular Graphics System, Schrodiner	https://pymol.org/2/
Prism 9	GraphPad	https://www.graphpad.com/scientific-software/prism/
MotionCor2	(Zheng et al., 2017)	https://emcore.ucsf.edu/ucsf-motioncor2
Coot	(Emsley et al., 2010)	https://www2.mrc-lmb.cam.ac.uk/personal/pemsley/coot/
UCSF Chimera	(Pettersen et al., 2004)	http://www.cgl.ucsf.edu/chimera
UCSF ChimeraX	(Goddard et al., 2018)	https://www.rbvi.ucsf.edu/chimerax/
PHENIX	(Adams et al., 2010)	http://www.phenix-online.org/
RELION 3.0	(Zivanov et al., 2018)	https://www3.mrc-lmb.cam.ac.uk/relion/
SerialEM	(Mastronarde, 2005)	http://bio3d.colorado.edu/SerialEM/
Schrödinger Suite 2018-1	Schrödinger, Inc.	https://www.schrodinger.com/